

**Bright spatially coherent beam from carbon-nanotube fiber field-emission cathode**Taha Y. Posos<sup>1,\*</sup>, Jack Cook,<sup>2</sup> and Sergey V. Baryshev<sup>1,†</sup><sup>1</sup>*Electrical and Computer Engineering, Michigan State University, Michigan 48824, USA*<sup>2</sup>*Cambridge University, Cambridge CB2 1TN, United Kingdom* (Received 27 December 2023; revised 6 May 2024; accepted 15 July 2024; published 7 August 2024)

Large-area carbon-nanotube (CNT) cathodes made from yarns, films, or fibers have long been promising as next-generation electron sources for high-power rf and microwave-vacuum-electronic devices. However, experimental evidence has highlighted that spatial incoherence of the electron beam produced by such cathodes impeded the progress toward high brightness CNT electron sources and their practical applications. Indeed, typically large-area CNT fibers, films, or textiles emit stochastically across their physical surface at large emission angles and with large transverse spread, meaning large emittance and hence low brightness. In this work, using high-resolution field-emission microscopy, we demonstrate that conventional electroplating of hair-thick CNT fibers followed by a femtosecond laser cutting, producing an emitter surface, solves the described incoherent emission issues extremely well. Strikingly, it was observed that the entire (within the error margin) cathode surface of a radius of approximately 75  $\mu\text{m}$  emitted uniformly (with no hot spots) in the direction of the applied electric field. The normalized cathode emittance, i.e., on the fiber surface, was estimated as 26-nm rad with brightness of  $>10^{16}$  A/m<sup>2</sup> rad<sup>2</sup> (or  $>10^7$  A m<sup>-2</sup> sr<sup>-1</sup> V<sup>-1</sup>) estimated for pulsed-mode operation.

DOI: [10.1103/PhysRevApplied.22.024017](https://doi.org/10.1103/PhysRevApplied.22.024017)**I. INTRODUCTION**

In the early 1990s, the carbon-nanotechnology revolution introduced a plethora of alternative advanced materials among which the carbon nanotube was notoriously attractive for making nanoscale field-effect devices, including vacuum devices. Many labs studied the effects associated with field emission from a single CNT or arrays with a counted number of isolated CNTs [1–6]. Control over fabrication and emission of single CNT field-emission devices was excellent and many field-emission devices were demonstrated, e.g., field-emission radio [7] or field-emission transistor [8], amplifier [9], and many others [5,6].

In order to increase the output power, macroscopic large-area CNT fibers, films, yarns, and fabrics started to be used to increase the operating currents from pico and nano to many amperes. Here, CNTs were thought to replace legacy velvets [10]. The multiple benefits of CNT fibers over legacy technology are low turn-on voltage and high emission current at relatively low operating electric field due to inherent high-field enhancement factor, and high electrical and thermal conductivities [11]. It was conventionally assumed that emission would be uniform, i.e., uniformity would translate from previously studied arrays

of counted CNTs to the large-area CNT fibers. However, recent studies that employed field-emission microscopy illustrated that emission is never uniform and moreover that the emission area is a function of the electric field (making it cumbersome for calculating current densities). Figure 1, reproduced from our past work [12], highlights another issue of the large transverse spread of the emitted beam where the beam lands on the imaging screen millimeters away from the physical location of the cathode source (blue circle) after traveling only a millimeter between the cathode and the anode. This clearly points out a very large emittance and therefore very low brightness, making CNT fiber cathodes impractical for applications like rf or microwave traveling-wave tubes (operating in GHz range), microscopy, and bright x-ray sources for medicine or active scanning. Another issue arises from that—because all the current emerges from a few active spots, it leads to local heating, microbreakdowns [12], and short-lived cathodes.

After experimenting with many fiber arrangements, we found that it is tiny singular fibrils (comprising braided fibers) that set loose due to thermal and field-related stress [12,13] and that eventually focus the field due to their high aspect ratio and become pointlike randomized intense electron emitters eventually exploding (seen as microbreakdowns) and repopulating surrounding areas with more new-born fibrils. This process repeats itself until the cathodes stops operating while emission always

\*Contact author: [posostah@msu.edu](mailto:posostah@msu.edu)†Contact author: [serbar@msu.edu](mailto:serbar@msu.edu)

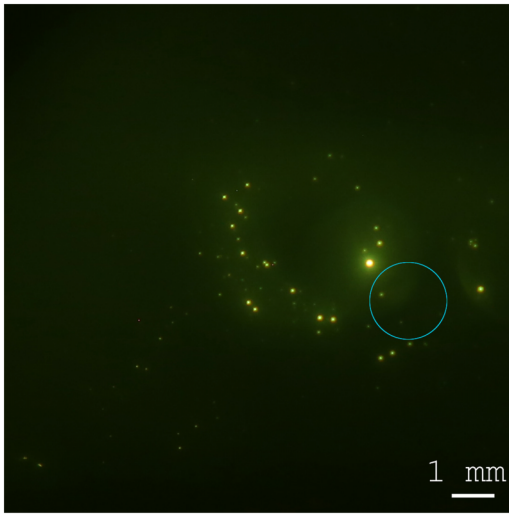


FIG. 1. Typical micrograph showing large beam transverse spread and nonuniformity. The blue circle marks the cathode’s position behind the imaging screen and its size.

look like a family of single-electron rays going in many directions that are not aligned with the desired main longitudinal propagation direction, such as in Fig. 1. To mitigate this issue, hypothesized to be the major problem, we study other cathode production technology where fibers are electroplated with Ni and laser cut; all to suppress the fibril occurrence and regeneration. Through experimental measurements and electrostatic and beam dynamics modeling, emission uniformity and beam brightness were analyzed.

## II. EXPERIMENTAL DETAILS

To prepare the field-emission CNT fiber cathodes, a commercially available CNT fiber from DexMat, Inc. was used. The fiber is made by a wet-spinning technology [11]—pregrown arrays of CNTs are dissolved in an acid to form a spinnable liquid dope that is extruded through a spinneret into coagulant bath to remove acid, and then dried in an oven. The resulting product is highly aligned and densely packaged CNTs in a form of a fiber. DexMat fibers have high electrical and thermal conductivity. Such fibers were shown to feature anisotropic field emission [14]. Emission takes place along the fiber (not from side walls), which is a great property allowing for control over emittance. Raman spectroscopy shows the G peak positions at  $1583\text{ cm}^{-1}$  suggesting rich crystalline graphitic content as expected from high-quality fibers [Fig. 2(a)].

To mitigate the described stray fibril problem, few fibers of the described kind were placed side by side and electroplated with Ni in an electrochemical bath and flush cut from the top to the required length of about 5 mm with a femtosecond micromachining laser beam. Then, it

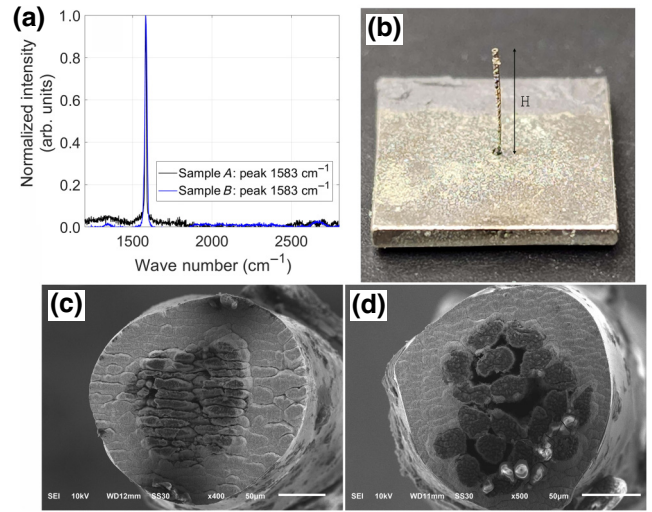


FIG. 2. (a) Raman spectra of the cathode surface showing a crystalline graphitic peak. The ratio of the G peak (approximately  $1600\text{ cm}^{-1}$ ) intensity to the D peak (approximately  $1300\text{ cm}^{-1}$ ) intensity is  $>20$ , which highlights high CNT crystallinity [15]. (b) Electroplated CNT fiber welded on a Ni base;  $H = 4.8\text{ mm}$  for sample *A* and  $H = 4.6\text{ mm}$  for sample *B*. (c),(d) SEM images of sample *A* and sample *B*, where scale bars are  $50\text{ }\mu\text{m}$ .

was welded on a  $1 \times 1\text{ in.}$  Ni base. The final fabricated structure can be seen in Fig. 2(b).

We tested two samples referred to as sample *A* and sample *B* through the rest of the paper. In sample *A* fibers were twisted and in sample *B* were not, i.e., simply placed along each others. As scanning electron microscopy (SEM) demonstrates in Fig. 2(c), additional fiber twisting enabled a dense core in sample *A*, while sample *B* [Fig. 2(d)] has visible voids between the individual fibers. Otherwise, both samples had a fiber core diameter of approximately  $150\text{ }\mu\text{m}$  and Ni shell thickness of approximately  $50\text{ }\mu\text{m}$ . Sample *A* and sample *B* have heights of  $4.8\text{ mm}$  and  $4.6\text{ mm}$ , respectively [see Fig. 2(b)]. Surface measurements by the Alicona 3D optical microscope revealed that the surface peak-to-peak roughness was approximately  $10\text{ }\mu\text{m}$ .

dc current tests and field-emission microscopy were performed in our custom field-emission microscope described in great detail in Ref. [16]. Images were processed by a custom image-processing algorithm FEpic described elsewhere [17]. The sample was placed across a Mo/YAG screen in a vacuum chamber, as shown in Fig. 3. The cathode and the chamber body were grounded and the screen was biased. Electrons striking the screen formed micrographs, which were captured by a camera behind the illumination screen. The bias voltage was swept up and down and the anode screen images were captured synchronously. All data acquisition was performed automatically using a controller and custom software [16].

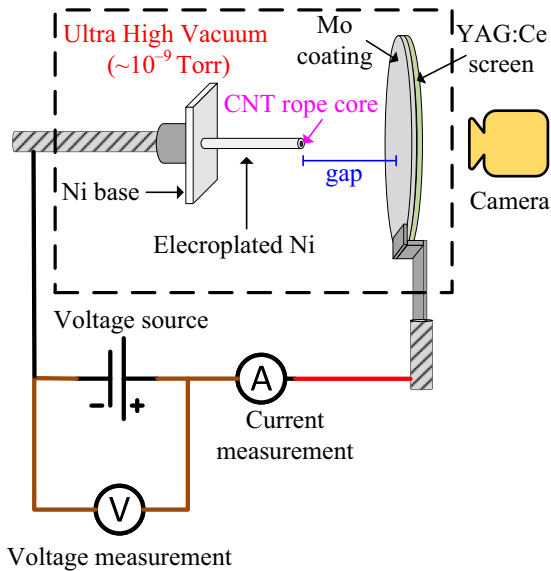


FIG. 3. Schematic of the dc measurement setup.

### III. FIELD-EMISSION IMAGING AND CONDITIONING

After the sample was installed and the gap was tuned using a doublet of two orthogonal optical microscopes, the physical location of the fiber is determined and labeled. To do that, the test chamber is illuminated. Because the imaging anode YAG screen is semitransparent, the location of the fiber can be immediately seen and captured by photographing. The core of the fiber is marked with a red circle for reference in Figs. 4(a) and 5(a).

After that, voltage is applied and field-emission images are taken concurrently with  $I$ - $V$  curves. Figure 4(b) shows the emission micrograph of sample *A*. The improvement is immediately obvious when compared with Fig. 1. First, the emission spot appears exactly at the optical projection of the cathode. This means beam-divergence angle is small, so emittance can be expected to be low. Second,

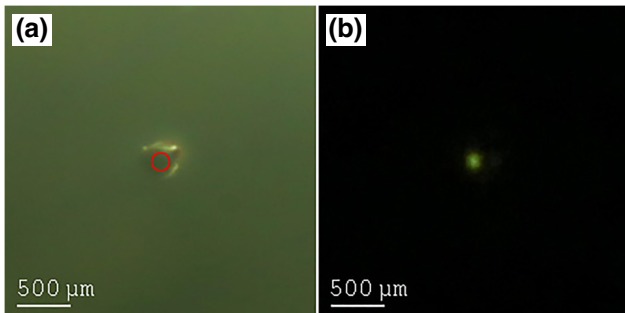


FIG. 4. (a) Sample *A* seen through the YAG screen when the lights are on in the chamber. Its fiber core is marked with a red circle. (b) Field emission (FE) micrograph of the same region at the gap of 200  $\mu\text{m}$ .

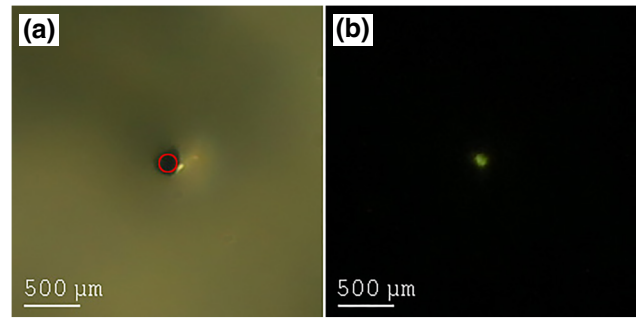


FIG. 5. (a) Sample *B* seen through the YAG screen when the lights are on in the chamber. Its fiber core is marked with a red circle. (b) FE micrograph of the same region at the gap of 200  $\mu\text{m}$ .

there is only a single spot and its size is comparable to the size of the fiber core—this is an indication of uniformity and small angular spread of the electron beam. The same exact behavior was observed for sample *B*, as given in Fig. 5. No evidence suggesting the stray fibril issue was observed for neither cathode. These results highlight that such a simple electroplating strategy is extremely effective at yielding emission uniformity and spatial coherence, thereby boosting the transverse beam brightness.

Figure 6 shows cathode conditioning  $I$ - $V$  curves for samples *A* and *B* at interelectrode gap of 200  $\mu\text{m}$ . Conditioning [12,18,19] or cycling, where the applied voltage is ramped up and down to a progressively higher number in every consecutive cycle until the desired operating current is achieved, is a crucial procedure to maximize field-emission cathode performance and ensure stability at the operating point.

We found that the electroplated fibers should be conditioned with small incremental steps to avoid adverse effects, such as sudden burn-down. Figure 6(a) demonstrates the case where the maximal field was doubled with respect to the previous conditioning cycle, such that the current went up from 3 to 22  $\mu\text{A}$ . Next, after completing the ramp down, Sample *A* stopped working completely, which was possibly due to applying electric power that exceeded that in the previous run by more than an order of magnitude. Its operation could not be rejuvenated by applying higher electric fields. This is unlike a conditioning scheme that was used for cathode *B* as shown in Fig. 6(b). The emission current was doubled at every conditioning cycle: up to 1  $\mu\text{A}$  and down to 0, then to 2  $\mu\text{A}$ , to 4  $\mu\text{A}$ , to 8  $\mu\text{A}$ , to 16  $\mu\text{A}$ , and finally to 32  $\mu\text{A}$ . By doing so, cathode *B* was conditioned *softly* (compared to sample *A*) maintaining and enhancing its performance: (i) the resulting operating field went up and doubled, reaching same exact value where cathode *A* burned down; (ii) turn-on field and field-enhancement factor remained nearly the same meaning that cathode *B* was conditioned to stably sustain higher local field.

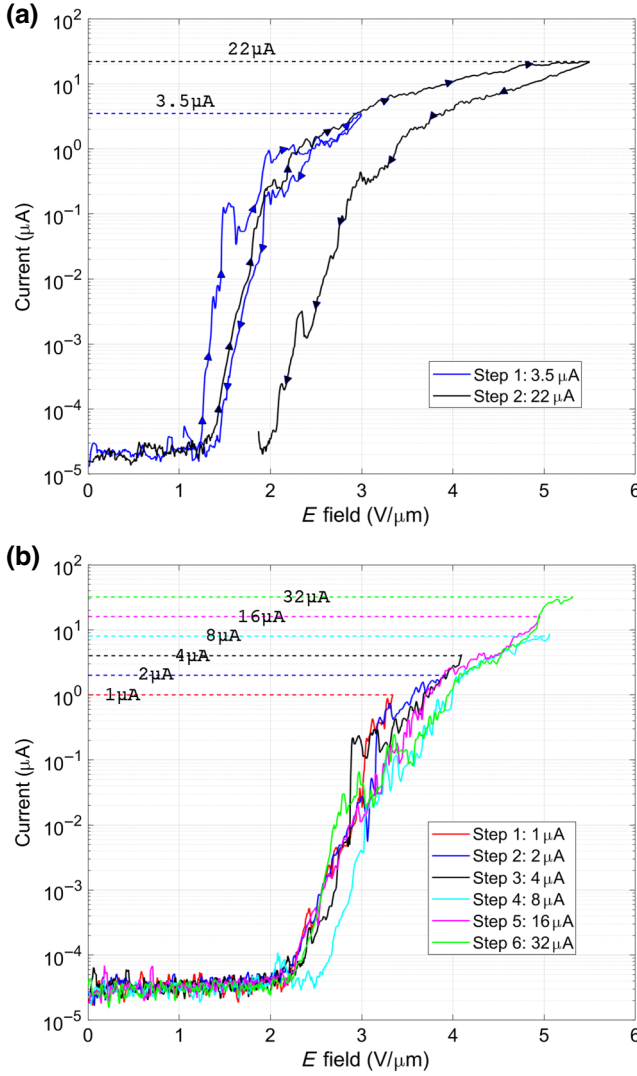


FIG. 6. (a) The conditioning scheme of sample *A*. Both ramp up and down curves are shown. There is a clear decrease in performance. (b) Conditioning scheme of sample *B*. Only ramp-up curves are shown. There is no considerable change in performance.

When it is compared to our past cathode designs, detailed in Ref. [12], they emit less at any given field. This is an expected result because (with stray fibrils mitigated) the field enhancement is reduced. However, turn-on fields are still very low, between 1 and 2.5 V/μm. Because the beam was tight suggesting high current density, we limited our measurements to between 10–100 μA as the power-density deposition at the imaging screen could attain above 1 kW/cm<sup>2</sup> at the voltage source limit of 1100 V, thereby literally drilling holes in it [20,21]. At 1100 V, sample *A* maxed out at 20 μA and sample *B* 30 μA, respectively. Again both cathodes had similar metrics. Having these metrics and qualitative results in mind, a step was taken

to carry out more quantitative analysis and calculate cathodes' emittance and brightness. All detailed in the next section.

#### IV. EMITTANCE AND BRIGHTNESS

In the phase space,  $(x, x')$ ,  $x$  is spatial position and  $x' = dx/dz = (dx/dt)/(dz/dt) = v_x/v_z$  is the slope of the trajectory from longitudinal centrosymmetric axis of each particle. Then, rms emittance  $\tilde{\epsilon}_x$  is defined as

$$\tilde{\epsilon}_x = \sqrt{\langle \Delta x^2 \rangle \langle \Delta x'^2 \rangle - \langle \Delta x \Delta x' \rangle^2}, \quad (1)$$

where  $\Delta x = x - \langle x \rangle$  and  $\Delta x' = x' - \langle x' \rangle$ . For a beam with cylindrical symmetry in  $(x, y)$  and  $(x', y')$  centered around zero,  $\langle x \rangle$  and  $\langle x' \rangle$  are zero. Then, Eq. (1) becomes

$$\tilde{\epsilon}_x = \sqrt{\langle x^2 \rangle \langle x'^2 \rangle - \langle x x' \rangle^2}. \quad (2)$$

rms emittance is a function of the beam energy as  $x'$  changes under acceleration, and is not useful while comparing beams at different energies. On the other hand, from Liouville's theorem [22], normalized emittance is a conserved quantity under acceleration as long as the beam is only subjected to conservative linear forces, so the rms emittance will be conserved under linear beam optical elements such as focusing solenoid and quadrupole. The relation between the rms emittance and normalized emittance [23] is given by

$$\epsilon_x^N = \gamma \beta \tilde{\epsilon}_x, \quad (3)$$

where  $\gamma = 1/\sqrt{1 - \beta^2}$  is the Lorentz factor and  $\beta = v/c$ . Because of acceleration, the longitudinal kinetic energy is dominant and  $v \approx v_z$ , and, in turn,  $\beta \approx v_z/c$ . In our case, also  $\gamma \approx 1$  because energy is  $\leq 1$  keV. By substituting  $\gamma$ ,  $\beta$ , and  $\tilde{\epsilon}_x$ ,

$$\epsilon_x^N = \frac{v_z}{c} \sqrt{\langle x^2 \rangle \left\langle \frac{v_x^2}{v_z^2} \right\rangle - \left\langle x \frac{v_x}{v_z} \right\rangle^2}. \quad (4)$$

Due to acceleration, the particles have approximately the same  $v_z$ , so it can be taken out of the averaging operator in Eq. (4). Then,

$$\begin{aligned} \epsilon_x^N &= \frac{v_z}{c} \sqrt{\langle x^2 \rangle \frac{\langle v_x^2 \rangle}{v_z^2} - \frac{\langle x v_x \rangle^2}{v_z^2}} \\ &= \sqrt{\langle x^2 \rangle \left\langle \frac{v_x^2}{c^2} \right\rangle - \left\langle x \frac{v_x}{c} \right\rangle^2}. \end{aligned} \quad (5)$$

In terms of  $(\beta_x, \beta_y) = (v_x/c, v_y/c)$ , Eq. (5) transforms

$$\epsilon_x^N = \sqrt{\langle x^2 \rangle \langle \beta_x^2 \rangle - \langle x \beta_x \rangle^2}. \quad (6)$$

In a special case, where  $x$  and  $\beta_x$  are uncorrelated,  $\langle x\beta_x \rangle = 0$ , then, Eq. (6) reduces to

$$\epsilon_x^N = \sqrt{\langle x^2 \rangle \langle \beta_x^2 \rangle} = \sigma_x \sqrt{\frac{\langle v_x^2 \rangle}{c^2}} = \sigma_x \sqrt{\frac{m_e \langle v_x^2 \rangle}{m_e c^2}}. \quad (7)$$

Mean-transverse energy (MTE),  $E_{\text{MTE}}$ , is  $\frac{1}{2}m_e \langle v^2 \rangle$ , where  $v^2 = v_x^2 + v_y^2$ . Because of the cylindrical symmetry in  $(v_x, v_y)$ ,  $E_{\text{MTE}} \approx \frac{1}{2}m_e \langle 2v_x^2 \rangle = m_e \langle v_x^2 \rangle$ . Then, Eq. (7) in terms of MTE is

$$\epsilon_x^N = \sigma_x \sqrt{\frac{E_{\text{MTE}}}{m_e c^2}}. \quad (8)$$

This form is especially useful at the cathode surface where momentum and position spaces are uncorrelated. It is noted, the correlation can also be removed at the beam waist when the beam is focused with proper beam optics [24].

By using the normalized emittance, the normalized transverse brightness,  $B_N$ , can be calculated as

$$B_N = \frac{2I}{\epsilon_x^N \epsilon_y^N}, \quad (9)$$

where  $I$  is the emitted current.  $\epsilon_x^N = \epsilon_y^N$  can be taken in cylindrical symmetry.

### A. Measurements and simulations

To compute emittance, the distribution of particles in  $x$  space and  $\beta_x$  space are needed [Eq. (6)]. Experiments and simulations were used together to obtain these values. Experiments formed a validation set to check simulation parameters. The experiments were as follows: the screen was moved away from the cathode progressively (Fig. 7). The voltage was set accordingly to maintain the current constant at 20 nA to enable a strong beam image signal but avoid additional beam expansion due to the vacuum-space-charge effect. A micrograph at each step is recorded (see Fig. 7). In Fig. 7, as expected, the beam expands transversely more as the interelectrode distance increases. The spots in the micrographs are Gaussian in nature, having an intense center and quickly fainting tails. To extract the transverse beam size from projected micrographs, each spot can be modeled mathematically as a cylindrically symmetric Gaussian ( $\sigma_x = \sigma_y$ ) as

$$p = A \exp\left(-\frac{(x - x_c)^2 + (y - y_c)^2}{2\sigma_x^2}\right) + C. \quad (10)$$

Here,  $(x, y)$  are the space dimensions,  $(x_c, y_c)$  are the coordinates of the peak,  $\sigma_x$  is the standard deviation,  $p$  is the intensity,  $A$  is the amplitude,  $C$  is the background offset

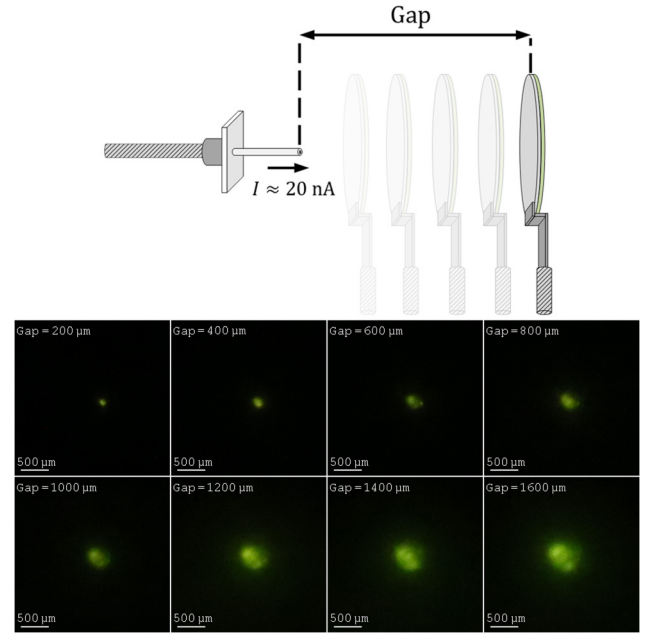


FIG. 7. The screen was moved away from the cathode progressively, thereby increasing the cathode-anode distance from 200 to 1600  $\mu\text{m}$  in 200- $\mu\text{m}$  intervals. The spot size at each position was measured (Fig. 8) and plotted in Fig. 9(a). The voltage was adjusted (630, 780, 860, 940, 970, 1040, 1070, and 1100 V for 200-, 400-, 600-, 800-, 1000-, 1100-, 1200-, 1400-, 1600- $\mu\text{m}$  gap, respectively) at each step to maintain the current constant at 20 nA so that the illumination of the screen was similar. The spot size increases as the distance increases because the beam has more time to expand. These measurements were used to validate GPT simulation parameters (Figs. 9 and 11).

[17]. The model parameters  $A$ ,  $\sigma_x$ , and  $C$  for each spot were computed with the least-squares fitting method. After fitting, the spot diameter was taken as  $2\sigma_x$ . An exemplary fitting done by FEpic [17] for the beam imaged at 200- $\mu\text{m}$  gap is presented in Fig. 8. The resulting dependence of the experimental spot size versus the cathode-anode distance is shown in Fig. 9(a) with blue triangles. The data in the figure is only for sample B. Because sample A burned down, studies similar to those presented in Fig. 7 could not be carried out.

The end-to-end beam dynamics simulations were performed in General Particle Tracer (GPT). The experimental growth rate was used to assess the realism of the simulated cathode surface and the simulated beam initialization. The procedure was as follows: the electric field maps were generated in COMSOL for each gap (Fig. 10). In COMSOL, the cathode geometry was set with a core diameter of 150  $\mu\text{m}$ , a shell thickness of 50  $\mu\text{m}$ , a height of 4.7 mm, and a periodic peak-to-peak surface roughness of 10  $\mu\text{m}$ , according to the measured dimensions using optical 3D microscopy. For the anode, a flat surface having the same diameter as the scintillator screen was used. The

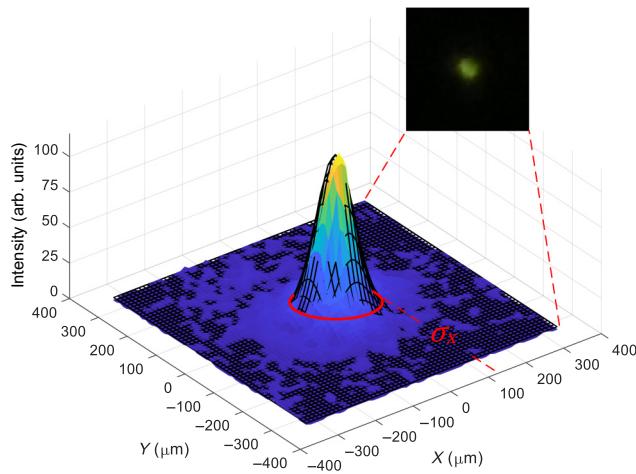


FIG. 8. The experimental spot size data for the 200- $\mu\text{m}$  gap (Fig. 7) is shown in  $(x, y)$  vs pixel intensity as a color surface. The plot reveals the Gaussian nature of the spot. One standard deviation from the center ( $\sigma_x$ ) is a good representation of the spot radius. The cylindrically symmetric Gaussian function expressed in Eq. (10) was fitted (the mesh surface shows the fit) to calculate experimental  $\sigma_x$ .

system was biased with the same voltages as in the experiments summarized in Fig. 7. The generated field maps were exported to GPT. An exemplary field distribution for 1-mm gap is shown in Fig. 10.

In GPT, the beam was initialized with a uniform circular distribution 150  $\mu\text{m}$  in diameter [Fig. 11(a)] in the coordinate space  $(x, y)$  and with 0-eV initial energy [Fig. 11(b)] in the momentum space  $(\beta_x, \beta_y) = (v_x/c, v_y/c)$ . The initialization in the coordinate space assumes a uniform emission over the entire CNT core surface. The simulations

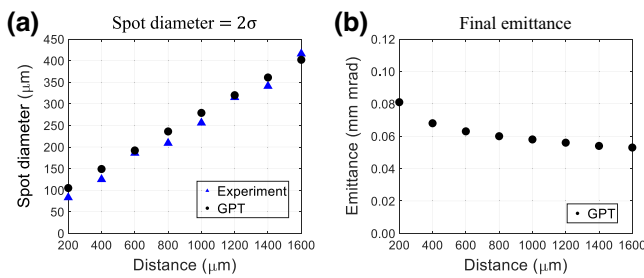


FIG. 9. Experimental vs simulated spot sizes (obtained with 0-eV initial MTE) were found to have good agreement [Fig. 9(a)], validating the claim of the uniform emission and the nonexistence of the stray emitters. The larger the gap, the larger the spot size, as the beam has more time to expand. GPT simulations enabled obtaining the distribution of final positions [Fig. 11(c)] and momenta [Fig. 11(d)], and hence calculating the beam emittance through Eq. (6). The emittance is reported in Fig. 9(b): as the interelectrode gap increases, the fringing field decreases, and the resulting emittance lowers to approximately 0.06 mm mrad.

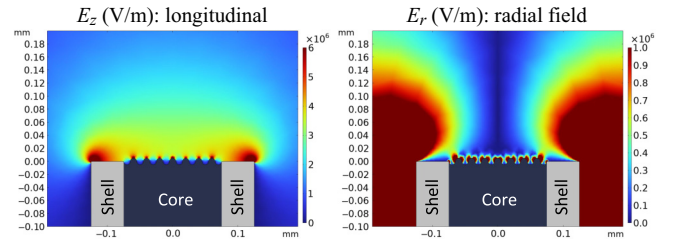


FIG. 10. The longitudinal and radial electric fields for 1-mm gap computed in COMSOL. The geometry has a core diameter of 150  $\mu\text{m}$ , a shell thickness of 50  $\mu\text{m}$ , a periodic peak-to-peak surface roughness of 10  $\mu\text{m}$ . It was calculated for an emitter post length of 4.7 mm. The same voltage of 970 V was applied as in the experiment (Fig. 7). The result shows a strong radial fringing field on the order of  $1 \times 10^6$  V/m. This is due to the high aspect ratio of the cathode. The fringing field is mainly on the shell but it also affects the field over the core due to close proximity. The periodic roughness also enhances the radial field (the red heart-shaped regions above the core region) but its effect disappears a few  $\mu\text{m}$  above the surface. The center has zero radial field due to the cylindrical symmetry.

were run for each gap and the final state of the beam was recorded at the screen position. The final distribution of particle positions and momenta for the gap of 1 mm are given in Figs. 11(c) and 11(d). From the final positions,  $\sigma_x$  were calculated as  $\sigma_x = \sqrt{\langle x^2 \rangle}$ , and  $2\sigma_x$  was taken as the beam diameter similar to the experimental case. The beam diameter is plotted in Fig. 9(a) with black circles. From the final position and momentum distributions,  $\langle x^2 \rangle$ ,  $\langle \beta_x^2 \rangle$  and  $\langle x\beta_x \rangle$  were calculated and substituted to Eq. (6) for emittance calculations. The emittance values are plotted in Fig. 9(b). From Fig. 9(b), the normalized emittance is around 0.06 mm mrad for longer distances.

From Fig. 9(a), the measured and simulated beam diameters are in very good agreement for every gap. This shows the simulated fields (Fig. 10) and beam initialization [uniform emission in Fig. 11(a)] are realistic. It forms a quantitative proof for uniform emission observed in Figs. 4 and 5. Secondly, because the simulated fields did not assume any high aspect ratio stray features over the surface, it proves that electroplating successfully suppressed the formation of the stray emitters causing abrupt beam expansion. Third, this realistic simulation also enabled obtaining the final momentum space [Fig. 11(d)] together with the coordinate space [Fig. 11(c)], making computation of the beam emittance [Fig. 9(b)] possible.

Taking the measured current (limited to 10–100  $\mu\text{A}$  due to extremely high power density in Fig. 6) as 50- $\mu\text{A}$  dc current and emittance as 0.06 mm mrad, the normalized brightness [Eq. (9)] in the dc mode is  $B_N = 2.8 \times 10^{10}$  A/m<sup>2</sup> rad<sup>2</sup>. The same very fibers could draw 1–10-A peak current in the pulsed mode with a pulse length of 100–300 ns [25]. Taking it as 5 A, in the pulsed mode (preferable mode in most VED HPM

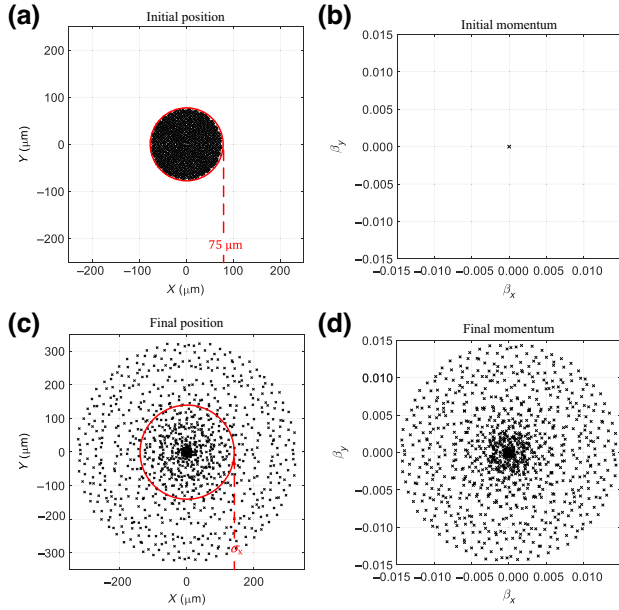


FIG. 11. In the coordinate space  $(x, y)$ , the beam was initialized with a uniform circular distribution [Fig. 11(a)] with the radius of the physical core ( $75 \mu\text{m}$ ). In the momentum space  $(\beta_x, \beta_y)$ , the initial MTE was set to 0 eV, so it is just a point at the origin [Fig. 11(b)]. The final particle positions and momenta distributions for 1-mm gap are shown in Figs. 11(c) and 11(d). Similar to the experimental case, the final spatial distribution [Fig. 11(c)] is Gaussian. One standard deviation ( $\sigma_x = \sqrt{\langle x^2 \rangle}$ ) from the center was taken as the final beam radius, which is plotted in Fig. 9(a) for each gap. From the final coordinate space [Fig. 11(c)] and momentum space [Fig. 11(d)], values of  $\langle x^2 \rangle$ ,  $\langle \beta_x^2 \rangle$ , and  $\langle x\beta_x \rangle$  were calculated. Then, from Eq. (6), the final emittance was calculated and plotted in Fig. 9(b). The radial fringing field (Fig. 10) is lowest at the core center and highest at the core edge. Therefore, while the beam center keeps its initial state, the beam edges expand [Fig. 11(c)] and gain transverse momentum [Fig. 11(d)] thus forming a Gaussian distribution.

applications), the brightness could attain a notable value on the order of  $B_N \approx 10^{15} \text{ A/m}^2 \text{ rad}^2$ . This (phase-space) brightness can be converted into geometrical brightness, a definition of brightness commonly employed in the electron-microscopy literature. The geometrical reduced brightness is defined as  $B_r^G = (dI/d\Omega)(1/U)(1/S_{\text{cathode}})$ , where  $\Omega$  is the solid angle,  $U$  is the voltage at which the current  $I$  is measured, and  $S_{\text{cathode}}$  is the emission area of the cathode. The calculations show that it could attain a value on the order of  $B_r^G \approx 10^7 \text{ A m}^{-2} \text{ sr}^{-1} \text{ V}^{-1}$  in the pulsed mode. This number is within the range obtained for single CNT emitters [26].

### B. Effect of initial energy

In GPT, the beam was also initialized with typical values of MTE (Fig. 12). A uniform circular distribution ( $\beta_x^{\text{max}} = \beta_y^{\text{max}}$ ) was used in the momentum space (Fig. 12). To set a

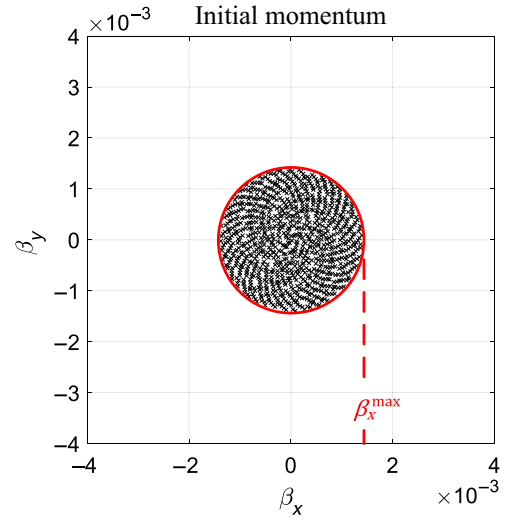


FIG. 12. The representation of the beam initialization with a nonzero initial MTE (coordinate-space initialization was the same as before). In momentum space, a circular uniform distribution with a radius of  $\beta_x^{\text{max}}$  was used. To set an intended initial MTE, the required  $\beta_x^{\text{max}}$  was calculated by Eq. (11). The results for initial  $E_{\text{MTE}} = 0, 0.25$  and  $1 \text{ eV}$  are plotted in Fig. 13.

specific initial MTE in the momentum space (Fig. 12), the radius of the distribution,  $\beta_x^{\text{max}}$ , was set as (see Appendix A for the derivation)

$$\beta_x^{\text{max}} = \sqrt{\frac{4 E_{\text{MTE}}}{m_e c^2}}. \quad (11)$$

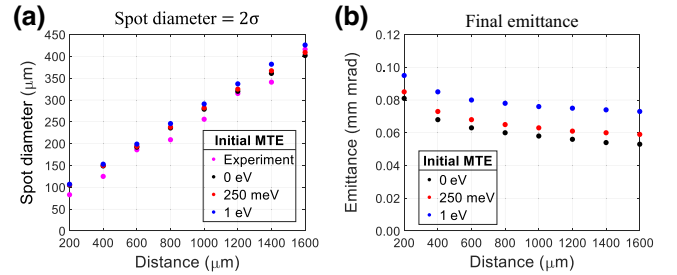


FIG. 13. It shows the effect of the initial MTE on the final state of the beam. In Fig. 13(a), the simulated spot size deviates further from the experimental case as the initial MTE increases. At 1 eV, the deviation from the experimental spot size becomes more pronounced (the 0-eV case is the closest one to the experimental case), so MTE must be  $< 1 \text{ eV}$  as expected for the given material [27]. So, the realistic final emittance has to be somewhere between the blue dots and the black ones in Fig. 13(b), which means the emittance is about  $0.08 \text{ mm mrad}$  as the worst-case scenario. The emittance is always lower for larger interelectrode distances, as the fringing field drops at larger anode-cathode distances.

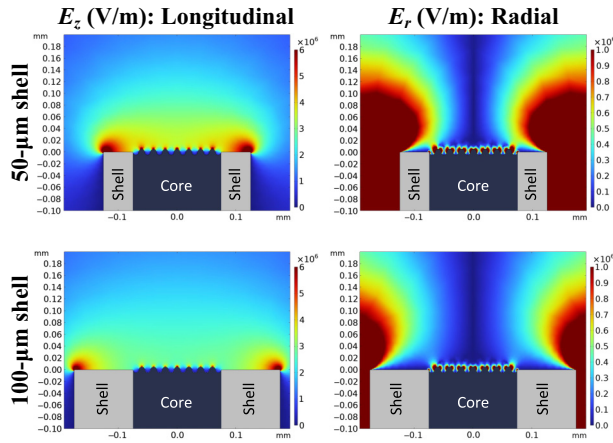


FIG. 14. The field maps generated for shell thicknesses of 50 and 100  $\mu\text{m}$  are shown for the 1-mm gap case. The thicker the shell, the smaller the effect of the radial field on the CNT core (the radial field is pushed to the edges). On the other hand, the reduction in the longitudinal field is not as strong. The radial and longitudinal fields in close proximity to the surface are not affected by the thickness change (red zones on the surface), as the surface roughness is the dominant factor there.

In the coordinate space, the beam was initialized in the same way as before [Fig. 11(a)]. The simulation results are plotted in Fig. 13.

From Fig. 13(a), as the initial MTE increases, the simulated spot size deviates more from the experimental one. At initial  $E_{\text{MTE}} = 1$  eV, the deviation is more prominent, indicating that the real initial MTE is expected to be under 1 eV. It also has to be a nonzero value in reality. Therefore, the real final emittance must be somewhere between blue dots and black ones in Fig. 13(b). The beam emittance 0.08 mm mrad can serve as an ultimate upper limit (worst-case scenario).

### C. Effect of shell thickness

In COMSOL, the shell thickness was doubled (100- $\mu\text{m}$  shell) and the resulting fields were recalculated for each gap (Fig. 14). In GPT, the beam was simulated with these alternative fields while initializing the beam as uniform with 0-eV initial energy [same as Fig. 11(a) and Fig. 11(b)]. The results are plotted in Fig. 15. Doubling the shell thickness reduces emittance [Fig. 15(b)] and spatial beam divergence [Fig. 15(a)] at any distance. The reason is that the thicker shell pushes the radial fringing field away from the core (Fig. 14), thereby its nonlinear radial force imposes lesser emittance growth. At 200- $\mu\text{m}$  gap, the reduction in the emittance is approximately 25% [Fig. 15(b)]. On the other hand, at 1600- $\mu\text{m}$  gap, the reduction in emittance is only 8% [Fig. 15(b)]. This difference arises because as the gap increases, the fringing field becomes more longitudinal (i.e., at an infinite gap, the

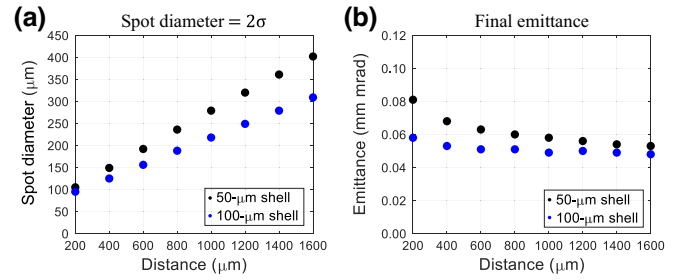


FIG. 15. The increase in the shell thickness leads to an improvement in the final beam emittance. The emittance decreases by almost 15% for the shorter gaps [Fig. 15(b)]. On the other hand, the benefit of having a thicker shell is less prominent for the larger anode-cathode gaps. The thicker shell reduces the fringing field on the core, resulting in less emittance growth [Fig. 15(b)] and less beam expansion [Fig. 15(a)] by its nonlinear radial force. However, the fringing field naturally decreases as the anode-cathode gap increases, leading to less impact from a thicker shell.

anode and cathode see each other as point sources, resulting in no radial field on the beam path at all), diminishing the contribution of a thicker shell.

In Fig. 16, surface fields 15  $\mu\text{m}$  above the surface were plotted for both of the shell thicknesses. Field emitters are built as high-aspect-ratio structures to enhance the field at the tip, and so to lower the operating voltages. The disadvantage is that the radial field gets enhanced too. So, the tip geometry requires optimization as the control over the radial field is essential to reduce emittance growth in field emitters. For this specific cathode, doubling the shell thickness reduces the radial field almost by half [Fig. 16(a)], which reduces the emittance by approximately 15% for shorter gaps [Fig. 15(b)]. At the same time, the longitudinal field [Fig. 16(b)] drops only by 20%. This means the cathode could perform even better with a thicker coating without needing to increase the operating voltage considerably. However, for larger gaps [Fig. 15(b)], it may not be worth increasing the operating voltage for the smaller effect of a thicker shell on emittance. A similar iterative analysis, as shown in Figs. 15(b) and 16, can be conducted to determine the optimal operating geometrical and electrical conditions for best injection for a particular electron-gun design.

### D. Intrinsic emittance

So far, only beam emittance—the emittance measured on the screen away from the cathode—has been considered. In this section, the cathode emittance, also called intrinsic emittance, is discussed. The intrinsic emittance is the emittance right at the cathode surface when the beam is launched. Because momenta and positions are not correlated at the cathode surface, Eq. (8) can be

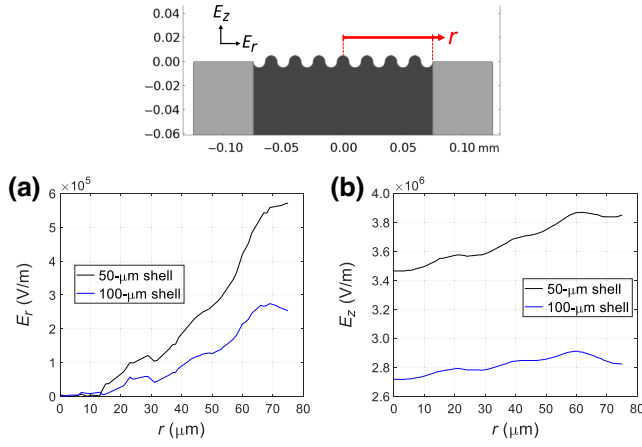


FIG. 16. The field for the gap of 1 mm and applied voltage of 970 V was sampled over the red line (15  $\mu\text{m}$  above the roughness peaks) and plotted for 50 and 100  $\mu\text{m}$  shell thicknesses. At 100- $\mu\text{m}$  shell, the radial field reduces almost in half [Fig. 16(a)], but the longitudinal field reduces only by 20% [Fig. 16(b)]. Therefore, by optimizing the shell design the emittance growth can be mitigated without appreciably increasing the operating voltage to attain the same amount of charge. As the red line is placed continuously closer to the cathode surface, the blue and black lines approach each other because the very surface fields are controlled by the roughness.

used for emittance calculation. With the uniform emission (proven in the previous sections), the initial beam radius can be taken as the core radius (75  $\mu\text{m}$ ). Then, for a uniform distribution,  $\sigma_x = \langle x^2 \rangle = x_{\text{max}}/2 = 75/2 = 37.5 \mu\text{m}$ . In another study of CNT fibers [27], electron energy distribution (EED) measurement reveals 250-meV initial MTE. This value can be taken as intrinsic and thermal MTE. From Fig. 13(a), the spot size starts to deviate strongly from the experimental data when MTE is set to 1 eV. Therefore, for the studied cathode the intrinsic MTE is  $<1$  eV. It must also be that MTE is  $>0$  as the statistical distribution of electrons inside the material in thermal equilibrium imposes it. Given our CNT material is made by the same production method as the one studied in Ref. [27], 250-meV intrinsic emittance is a good approximation. Then, by taking  $\sigma_x = 37.5 \mu\text{m}$  and  $E_{\text{MTE}} = 250$  meV, from Eq. (8), the intrinsic emittance becomes  $\epsilon_x^{\text{N}} = 0.026$  mm mrad = 26 nm rad. Using this value and the measured 50- $\mu\text{A}$  dc current, the cathode brightness is  $B_{\text{N}} = 1.5 \times 10^{11}$  A/m<sup>2</sup> rad<sup>2</sup> in dc mode. Assuming the fiber gives approximately 5 A peak current in the pulsed mode [25], the cathode brightness could attain a notable value on the order of  $B_{\text{N}} \approx 10^{16}$  A/m<sup>2</sup> rad<sup>2</sup>. This number is outstanding and is comparable with brightness metrics in the state-of-the-art microwave and rf accelerator injectors [28].

In photoemission, the intrinsic emittance is a key metric determining the beam quality. As photocathodes are designed to be flat (so the fields are linear and normal to the

surface), the emittance is conserved. Therefore, the laser spot size and intrinsic MTE of the cathode material have special significance in photoemission. Regarding nonlinear effects causing emittance growth, the photoemission literature generally focuses on the space-charge effect or radial field on the surface created either by surface roughness [29–31] or work-function variation over the cathode surface [32–34]. Studies showed that the radial field created by these surface nonuniformities could increase the emittance by up to 30% [30,31,34].

In the present study, the emittance on the screen (approximately 0.06 mm mrad) is approximately 2.3 times larger than the intrinsic one (approximately 0.026 mm mrad). This growth is not only a result of the surface roughness. In field emission, the cathode must be built as a sharp post. Therefore, the fringing radial field on the surface is inevitable (Fig. 10). It appears that the fringing field is the major factor causing the emittance growth (Figs. 13 and 14). The effect of the local fringing field caused by the surface roughness quenches quickly, a few  $\mu\text{m}$  away from the surface (Fig. 10). On the other hand, the effect of the global fringing field caused by emitter edge boundaries has a dramatic influence on the beam over longer distances (Fig. 10). Hence, the effect of intrinsic emittance is buried by the emittance growth due to external factors. Nevertheless, since intrinsic emittance represents the ultimate minimum that cannot be reduced by any linear beam optics or any adjustment to the shell thickness, it is useful to have an estimate of it.

## V. CONCLUSION

In conclusion, we presented a simple and efficient field-emission cathode design where CNT fiber core was plated with a nickel shell. This design had two functions. First, it compresses the core, and provides mechanical strength thereby preventing stray fibril formation during conditioning and operation. Second, such a design (while slightly reducing field enhancement and increasing turn-on field) reduces the fringing field on the CNT fiber and therefore the defocusing radial field.

As field-emission microscopy directly demonstrated, both tested cathodes featured excellent spatially coherent emission. Field-emission microscopy aided by image processing and beam dynamics simulations confirmed that the entire fiber core of 150  $\mu\text{m}$  in diameter actively and uniformly emitted electrons, as well as enabled phase-space analysis. All of these combined allowed the observed emission coherence to be quantified through calculating emittance and brightness. The extremely low emittance resulting in record brightness highlights a simple and practical path forward for the CNT fiber technology that has long been expected to advance high-frequency vacuum power devices but had limited success due to low brightness.

Finally, it was demonstrated that the nanoscopic single CNT cathode technology can be translated to the macroscopic fiber CNT level in terms of emission uniformity. In other words, spatial coherence and uniformity (intrinsic to a single CNT emitter) can be achieved in a CNT fiber comprised out of billions of single CNTs. The obtained brightness figures of merit further confirm this technology translation in that ultimate single CNT emitter brightness is feasible to attain for CNT fiber cathodes.

### ACKNOWLEDGMENTS

The authors would like to thank Dr. Steven Fairchild of AFRL and Dr. Nathaniel Lockwood of AFOSR for facilitating samples acquisition. We would like to thank Tanvi Nikhar for Raman measurement. This material is based upon work supported by the U.S. Department of Energy, Office of Science, Office of High Energy Physics under Award No. DE-SC0020429.

### APPENDIX: MEAN TRANSVERSE ENERGY OF A UNIFORM CIRCULAR DISTRIBUTION IN MOMENTUM SPACE

A uniform circular distribution with a radius of  $\beta_x^{\max}$  in momentum space is given in Fig. 17(a). We can define another variable  $\beta$  such that  $\beta^2 = \beta_x^2 + \beta_y^2$ . Then, the probability distribution function (PDF) of  $\beta$  is the linear curve in Fig. 17(b). The proof is as follows: assume the three concentric red circles in Fig. 17(a) dividing the momentum space into three regions. The number of particles inside a region is proportional to the area of the region. So, the probability of finding a particle in the innermost region ( $0 < \beta < \beta_x^{\max}/3$ ) is  $\frac{1}{9}$ , in the middle region ( $\beta_x^{\max}/3 < \beta < 2\beta_x^{\max}/3$ ) is  $\frac{3}{9}$ , and in the outermost region ( $2\beta_x^{\max}/3 < \beta < \beta_x^{\max}$ ) is  $\frac{5}{9}$ . In the PDF curve [Fig. 17(b)], the area under the curve for  $0 < \beta < \beta_x^{\max}/3$  is  $\frac{1}{9}$ , for  $\beta_x^{\max}/3 < \beta < 2\beta_x^{\max}/3$  is  $\frac{3}{9}$ , for  $2\beta_x^{\max}/3 < \beta < \beta_x^{\max}$  is  $\frac{5}{9}$ ; and the total area is 1. So, the PDF in Fig. 17(b) models the distribution in Fig. 17(a) correctly.

From Fig. 17(b), analytically the PDF is

$$\rho(\beta) = \begin{cases} \frac{2}{(\beta_x^{\max})^2} \beta, & \text{if } 0 < \beta < \beta_x^{\max}; \\ 0, & \text{otherwise.} \end{cases} \quad (\text{A1})$$

Then, the average of  $\beta^2$  is

$$\begin{aligned} \langle \beta^2 \rangle &= \int_{-\infty}^{\infty} \beta^2 \rho(\beta) d\beta \\ &= \frac{1}{2} (\beta_x^{\max})^2. \end{aligned} \quad (\text{A2})$$

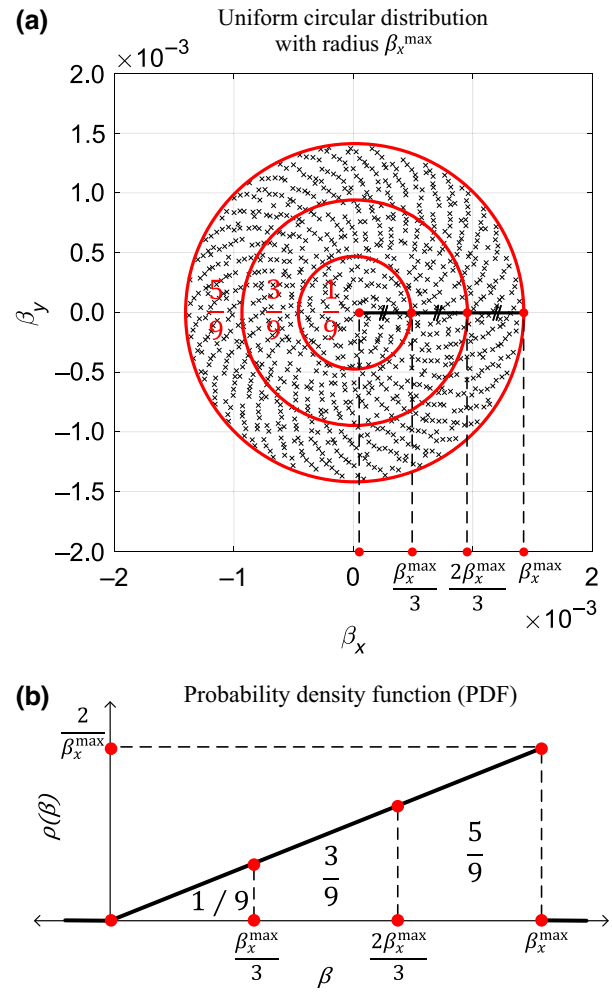


FIG. 17. A uniform circular distribution [Fig. 17(a)] with radius  $\beta_x^{\max}$  in momentum space ( $\beta_x, \beta_y$ ) forms a linear PDF curve [Fig. 17(b)] with respect to  $\beta$  ( $\beta^2 = \beta_x^2 + \beta_y^2$ ). This can be understood by dividing the momentum space into virtual regions with the red circles in Fig. 17(a). By considering the number of particles inside each region [Fig. 17(a)], the probability of finding a particle in the innermost region is  $1/9$ , in the middle region is  $3/9$ , and in the outermost region is  $5/9$ . The area under PDF [Fig. 17(b)] for the range of  $\beta$  corresponding to the innermost region is  $1/9$ , for the range of  $\beta$  corresponding to the middle region is  $3/9$ , and for the range of  $\beta$  corresponding to the outermost region is  $5/9$ . This shows that the PDF function [Fig. 17(b)] accurately represents the uniform distribution [Fig. 17(a)].

By definition, MTE is

$$\begin{aligned} E_{\text{MTE}} &= \frac{1}{2} m_e c^2 \langle \beta_x^2 + \beta_y^2 \rangle \\ &= \frac{1}{2} m_e c^2 \langle \beta^2 \rangle \\ &= \frac{1}{4} m_e c^2 (\beta_x^{\max})^2. \end{aligned} \quad (\text{A3})$$

So,

$$\beta_x^{\max} = \sqrt{\frac{4 E_{\text{MTE}}}{m_e c^2}}. \quad (\text{A4})$$

This concludes the derivation of Eq. (11).

- 
- [1] K. A. Dean and B. R. Chalamala, Field emission microscopy of carbon nanotube caps, *J. Appl. Phys.* **85**, 3832 (1999).
- [2] E. Minoux, O. Groening, K. B. K. Teo, S. H. Dalal, L. Gangloff, J.-P. Schnell, L. Hudanski, I. Y. Y. Bu, P. Vincent, P. Legagneux, G. A. J. Amaratunga, and W. I. Milne, Achieving high-current carbon nanotube emitters, *Nano Lett.* **5**, 2135 (2005).
- [3] N. De Jonge, Y. Lamy, K. Schoots, and T. H. Oosterkamp, High brightness electron beam from a multi-walled carbon nanotube, *Nature* **420**, 393 (2002).
- [4] S. T. Purcell, P. Vincent, C. Journet, and V. T. Binh, Hot nanotubes: Stable heating of individual multiwall carbon nanotubes to 2000 K induced by the field-emission current, *Phys. Rev. Lett.* **88**, 105502 (2002).
- [5] K. Teo, R. Lacerda, M. Yang, A. Teh, L. Robinson, S. Dalal, N. Rupesinghe, M. Chhowalla, S. Lee, D. Jefferson, *et al.*, Carbon nanotube technology for solid state and vacuum electronics, *IEE Proc.-Circ. Dev. Syst.* **151**, 443 (2004).
- [6] Y. Li, Y. Sun, and J. Yeow, Nanotube field electron emission: Principles, development, and applications, *Nanotechnology* **26**, 242001 (2015).
- [7] K. Jensen, J. Weldon, H. Garcia, and A. Zettl, Nanotube radio, *Nano Lett.* **7**, 3508 (2007).
- [8] Y. Wong, W. Kang, J. Davidson, B. Choi, W. Hofmeister, and J. Huang, Field emission triode amplifier utilizing aligned carbon nanotubes, *Diam. Relat. Mater.* **14**, 2069 (2005).
- [9] Y. M. Wong, W. P. Kang, J. L. Davidson, D. V. Kerns, J. Huang, and K. F. Galloway, Characterization and CMRR modeling of a carbon-nanotube field-emission differential amplifier, *IEEE Trans. Electron Devices* **56**, 738 (2009).
- [10] D. Shiffler, S. Fairchild, W. Tang, B. Maruyama, K. Golby, M. LaCour, M. Pasquali, and N. Lockwood, Demonstration of an acid-spun single-walled nanotube fiber cathode, *IEEE Trans. Plasma Sci.* **40**, 1871 (2012).
- [11] N. Behabtu, C. C. Young, D. E. Tsentlovich, O. Kleinerman, X. Wang, A. W. K. Ma, E. A. Bengio, R. F. ter Waarbeek, J. J. de Jong, R. E. Hoogerwerf, S. B. Fairchild, J. B. Ferguson, B. Maruyama, J. Kono, Y. Talmon, Y. Cohen, M. J. Otto, and M. Pasquali, Strong, light, multifunctional fibers of carbon nanotubes with ultrahigh conductivity, *Science* **339**, 182 (2013).
- [12] T. Y. Posos, S. B. Fairchild, J. Park, and S. V. Baryshev, Field emission microscopy of carbon nanotube fibers: Evaluating and interpreting spatial emission, *J. Vac. Sci. Technol. B* **38**, 024006 (2020).
- [13] S. B. Fairchild, J. Boeckl, T. C. Back, J. B. Ferguson, H. Koerner, P. T. Murray, B. Maruyama, M. A. Lange, M. M. Cahay, N. Behabtu, C. C. Young, M. Pasquali, N. P. Lockwood, K. L. Averett, G. Gruen, and D. E. Tsentlovich, Morphology dependent field emission of acid-spun carbon nanotube fibers, *Nanotechnology* **26**, 105706 (2015).
- [14] S. B. Fairchild, T. A. de Assis, J. H. Park, M. Cahay, J. Bulmer, D. E. Tsentlovich, Y. S. Ang, L. K. Ang, J. Ludwick, T. C. Back, and M. Pasquali, Strongly anisotropic field emission from highly aligned carbon nanotube films, *J. Appl. Phys.* **129**, 125103 (2021).
- [15] D. E. Tsentlovich, R. J. Headrick, F. Mirri, J. Hao, N. Behabtu, C. C. Young, and M. Pasquali, Influence of carbon nanotube characteristics on macroscopic fiber properties, *ACS Appl. Mater. Interfaces* **9**, 36189 (2017).
- [16] S. S. Baturin and S. V. Baryshev, Electron emission projection imager, *Rev. Sci. Instrum.* **88**, 033701 (2017).
- [17] T. Y. Posos, O. Chubenko, and S. V. Baryshev, Confirmation of transit time-limited field emission in advanced carbon materials with a fast pattern recognition algorithm, *ACS Appl. Electron. Mater.* **3**, 4990 (2021).
- [18] R. A. Millikan and C. F. Eyring, Laws governing the pulling of electrons out of metals by intense electrical fields, *Phys. Rev.* **27**, 51 (1926).
- [19] J. Shao, M. Schneider, G. Chen, T. Nikhar, K. K. Kovi, L. Spentzouris, E. Wisniewski, J. Power, M. Conde, W. Liu, and S. V. Baryshev, High power conditioning and benchmarking of planar nitrogen-incorporated ultrananocrystalline diamond field emission electron source, *Phys. Rev. Accel. Beams* **22**, 123402 (2019).
- [20] K. M. Jasim, R. Rawlings, and D. West, Operating regimes for laser surface engineering of ceramics, *J. Mater. Sci.* **27**, 1937 (1992).
- [21] A. Klimov, A. Zenin, Y. Yushkov, and E. Oks, Electron beam evaporation of alumina ceramics at forevacuum pressure range, *AIP Conf. Proc.* **1772**, 040003 (2016).
- [22] J. W. Gibbs, *Elementary Principles in Statistical Mechanics* (Cambridge University Press, Cambridge, 2010).
- [23] K. T. McDonald and D. P. Russell, in *Frontiers of Particle Beams; Observation, Diagnosis and Correction* (Springer Berlin, Berlin, 1989), p. 122.
- [24] J. D. Jarvis, Development of high-brightness electron sources for free-electron lasers, Ph.D. thesis, Vanderbilt University (2009), <https://www.proquest.com/docview/898735436>.
- [25] S. B. Fairchild, P. T. Murray, S. Portillo, and G. Dion, in *21st International Conference on Vacuum Electronics (IVEC)* (IEEE, Monterey, California, 2020), p. 19.
- [26] N. de Jonge, M. Allieux, J. T. Oostveen, K. B. K. Teo, and W. I. Milne, Optical performance of carbon-nanotube electron sources, *Phys. Rev. Lett.* **94**, 186807 (2005).
- [27] T. C. Back, G. Gruen, J. Park, P. T. Murray, J. Ludwick, M. Cahay, and S. B. Fairchild, Electron emission characteristics of wet spun carbon nanotube fibers, *AIP Adv.* **9**, 065319 (2019).
- [28] J. B. Rosenzweig, A. Cahill, V. Dolgashev, C. Emma, A. Fukasawa, R. Li, C. Limborg, J. Maxson, P. Musumeci, A. Nause, R. Pakter, R. Pompili, R. Roussel, B. Spataro, and S. Tantawi, Next generation high brightness electron beams from ultrahigh field cryogenic rf photocathode sources, *Phys. Rev. Accel. Beams* **22**, 023403 (2019).
- [29] Y. Y. Lau, Effects of cathode surface roughness on the quality of electron beams, *J. Appl. Phys.* **61**, 36 (1987).
- [30] M. Krasilnikov, in *Proceedings of FEL 2006 Conference* (JACoW Publishing, Berlin, 2006), p. 583.

- [31] Z. Zhang and C. Tang, Analytical study on emittance growth caused by roughness of a metallic photocathode, *Phys. Rev. ST Accel. Beams* **18**, 053401 (2015).
- [32] S. Karkare and I. Bazarov, Effects of surface nonuniformities on the mean transverse energy from photocathodes, *Phys. Rev. Appl.* **4**, 024015 (2015).
- [33] G. S. Gevorkyan, S. Karkare, S. Emamian, I. V. Bazarov, and H. A. Padmore, Effects of physical and chemical surface roughness on the brightness of electron beams from photocathodes, *Phys. Rev. Accel. Beams* **21**, 093401 (2018).
- [34] H. J. Qian, C. Li, Y. C. Du, L. X. Yan, J. F. Hua, W. H. Huang, and C. X. Tang, Experimental investigation of thermal emittance components of copper photocathode, *Phys. Rev. ST Accel. Beams* **15**, 040102 (2012).